Copyright © 2010 Tech Science Press CMES, vol.63, no.2, pp.137-161, 2010

Numerical Simulation of Fluid Induced Vibration of Graphenes at Micron Scales

Y. Inoue[1], R. Kobayashi[1], S. Ogata[1] and T. Gotoh[1]

Abstract: Vibration of a single graphene and a pair of graphenes at micro meter scale induced by air flow is numerically simulated and examined by using a hybrid computational method starting from a microscopic level of description for the graphene. In order to bridge a huge gap in spatial and time scales in their motions, the carbon atoms of the graphene are represented by a small number of coarse grained particles, the fluid motion is described by the lattice Boltzmann equation and the momentum exchange at the boundary is treated by the time averaged immersed boundary method. It is found that a single graphene with attack angle 60° and 90° to the flow direction begins to bend downstream with oscillation after release and tends to attain an equilibrium form, but the oscillation amplitudes for 30° increases in time. Also found is that when the separation distance of a pair of graphenes increases, the oscillation amplitudes become larger and chaotic and they collide each other, and the vorticity fields also tend to develop complex pattern. Strain distribution inside the graphene is also computed. Possibility to use the present system as a flow sensor and further development of the hybrid computational method are discussed.

Keywords: Microfluidics, coarse graining particle, lattice Boltzmann method, graphene, vibration, multi-scale multi-physics

1 Introduction

Microfluidics has been one of the most actively studied fields and attracting much attention. With progress in experimental technique and instruments the characteristic length and time scales of fluid devices such as flow pump, flow meter, mixer and so on are reaching micro meter or even nano meter scale, and developments of more efficient and smaller fluid devices are indispensable for the next generation MEMS and NEMS (Micro (or Nano)-Electro Mechanical System) [Kaabi, Kaabi, Sakly, and AbdelMalek (2007); Benvenuto, Guarnieri, Lorenzelli, Collini, Decarli,

[1] Nagoya Inst. Tech., Nagoya, Japan and JST-CREST

Adami, Potrich, Canteri, and Pederzolli (2008); Zhang, Ruan, Wang, Zhou, Wang, and Liu (2010)]. In the study of fluid devices at very small scales, the surface phenomena such as contact angle, slip velocity, surface roughness, chemical reaction, thermal noise, and the molecular structure of solid and fluid are important factors in designing and fabricating those devices, and understanding of interaction between fluid and solid at the interface between two phases by taking into account of these factors is highly demanding.

In this paper we focus on the mechanical aspects of the fluid-solid interaction at micro or submicron scales. For this purpose, however, it is not trivial whether the conventional continuum approaches using macroscopic parameters such as elastic constant and heat conductivity are sufficient to accurately describe the behavior of solid and the interaction between the two phases at mesoscale (micron to submicron scale) [Yan, He, Zhang, and Wang (2007)]. For example, graphene is a mono layer of carbon atoms of the hexagonal crystal structure and has been attracting great interest due to its unique characteristics such as large electron transfer, spin transfer, mechanical stability and strength, suggesting a wide range of applications as electronic devices [Novoselov, Geim, Morozov, Jiang, Zhang, Dubonos, Grigorieva, and Firsov (2004)]. Because of its crystalline structure, anisotropy in various material characteristics might be expected. Also the graphene is so easily bent that it would be used to make a nano scale flow sensor or driver by further advancing the fabrication techniques [Kondo, Sato, and Awano (2008)], but neither precise response to the external forces nor the elastic constants at the mesoscale are well known [Yan, He, Zhang, and Wang (2007)]. This motivates us to numerically simulate the interaction between the flow field and graphenes from the microscopic level, which is a multi-scale multi-physics problem because there exists a huge gap in their characteristic spatial and time scales.

We have developed a hybrid computational method to bridge over this huge gap in scales of motion [Inoue, Tanaka, Kobayashi, Ogata, and Gotoh (2008); Ogata, R. Kobayashi, and Gotoh (2009)] in which the interaction between fluid and hypothetical elastic rods composed of argon atoms in two dimensions is numerically simulated. Degrees of freedom of a large number of argon atoms are reduced to those of a small number of coarse grained particles (CGPs) by taking the thermal average of the Hamiltonian of the argon atoms under a constraint to a subset of the argon atoms (reduction in spatial scale), and the fluid motion is expressed in terms of the lattice Boltzmann equation (LBE). Momentum exchange at the interface is accomplished by coarse graining the immersed boundary method (IBM) in time domain (reduction in time scale). The hybrid method has successfully been applied to the problems of the interaction between the rods and fluid in two dimensions and shown that a collective motion of an array of the elastic rods excited by the

Rayleigh wave can generate a systematic flow in the opposite direction to that of the Rayleigh wave propagation, suggesting a flow driver [Benvenuto, Guarnieri, Lorenzelli, Collini, Decarli, Adami, Potrich, Canteri, and Pederzolli (2008)].

The aim of the present study is to further develop the above hybrid computational method for the problem of interaction between the graphenes and air flow in three dimensions. We analyze the motion of a single graphene and a pair of graphenes which are attached on the flat plate and set in a steady air flow. We examine how the graphene responds to the flow, and analyze the flow field and the strain distribution inside the graphene. The paper is organized as follows. In Section 2, the hybrid computational method by using CGP, LBE, and IBM is explained, and Section 3 describes the numerical conditions and the simulation results. In Section 4, we summarize the results and discuss the various aspects of the present method for the future development.

2 Hybrid computational method

2.1 Coarse grained particle method

Although the theory for the present hybrid computational method has been described in [Inoue, Tanaka, Kobayashi, Ogata, and Gotoh (2008)], we explain it with emphasis on the matching conditions of the spatial and time scales of motions because the present paper studies the case with more reality (graphene in the air flow in three dimensions) than before and because we believe that the idea and description of the method have been refined and become more precise.

The graphene is a single layer of carbon atoms connected by sp^2-bond and the characteristic length of a unit cell is of the order of 10^{-10} [m] and characteristic time of atomic vibration is 10^{-14} [s] [Novoselov, Geim, Morozov, Jiang, Zhang, Dubonos, Grigorieva, and Firsov (2004)]. On the other hand, the fluid motion is a collective motion of a large number of fluid molecules at submicron or larger scales. In order to numerically simulate the coupling of the fluid and the very small graphene from the microscopic view point, it is indispensable to reduce the degrees of freedom of atoms consisting the crystalline system. For this purpose we use the coarse grained particle (CGP) method which has been invented by Rudd and Broughton [Rudd and Broughton (1998, 2005)] and developed also by Ogata and his group [Kobayashi, Nakamura, and Ogata (2008a,b); Ogata, R. Kobayashi, and Gotoh (2009)]. Here we briefly describe the method, and its details and numerical performance can be seen in Refs. [Kobayashi, Nakamura, and Ogata (2008a); Ogata, R. Kobayashi, and Gotoh (2009)].

In the CGP method for the solid material with crystalline structure, the Hamiltonian

of the carbon atoms under the phonon approximation is assumed to be given by

$$H = \sum_{\alpha}^{N} \frac{\boldsymbol{p}_{\alpha}^{2}}{2m_{\alpha}} + \sum_{\alpha,\beta}^{N} \frac{1}{2} \boldsymbol{u}_{\alpha} \boldsymbol{D}_{\alpha\beta} \boldsymbol{u}_{\beta}, \tag{1}$$

where m_α, $\boldsymbol{u}_\alpha$, and $\boldsymbol{p}_\alpha$ are the mass, the displacement vector, and the momentum of atom α, respectively, and $\boldsymbol{D}_{\alpha\beta}$ is the dynamical matrix between atoms α and β. In order to reduce the degrees of freedom of N carbon atoms, the Hamiltonian H of the carbon atoms is statistically projected onto Hamiltonian H_{CG} of a small number ($N_{\mathrm{CG}} \ll N$) of CGPs by taking the thermal average

$$H_{\mathrm{CG}} = \frac{1}{Z} \left(\prod_{\alpha}^{N} \iint d\boldsymbol{u}_{\alpha} d\boldsymbol{p}_{\alpha} \right) H \exp\left(-\frac{H}{k_{\mathrm{B}} T} \right) \Delta \tag{2}$$

under the constraints

$$\Delta \equiv \prod_{i}^{N_{\mathrm{CG}}} \delta \left(\boldsymbol{U}_i - \sum_{\alpha}^{N_{\mathrm{C}}} \phi_{i,\alpha} \boldsymbol{u}_{\alpha} \right) \delta \left(\dot{\boldsymbol{U}}_i - \sum_{\alpha}^{N_{\mathrm{C}}} \phi_{i,\alpha} \frac{\boldsymbol{p}_{\alpha}}{m_{\alpha}} \right), \tag{3}$$

where $\delta(x)$ is Dirac's delta function, Z the partition function, k_B the Boltzmann constant, T the absolute temperature. The function $\phi_{i,\alpha}$ is a weight function which relates $\boldsymbol{U}_i$ to $\boldsymbol{u}_\alpha$ and corresponds to the inverse of the shape function used in the finite element method, and $N_{\mathrm{C}} (< N)$ is the number of the carbon atoms inside a spatial domain whose linear dimension is a few times larger than that of the mean separation distance of CGPs. Since the Hamiltonian H is a quadratic in $\boldsymbol{u}$ and $\boldsymbol{p}$, H_{CG} can be computed analytically as

$$H_{\mathrm{CG}} = H_{\mathrm{int}} + \frac{1}{2} \sum_{i,j}^{N_{\mathrm{CG}}} \left(\boldsymbol{P}_i \boldsymbol{M}_{ij}^{-1} \boldsymbol{P}_j + \boldsymbol{U}_i \boldsymbol{K}_{ij} \boldsymbol{U}_j \right), \tag{4}$$

$$H_{\mathrm{int}} \equiv 3 (N - N_{\mathrm{CG}}) k_{\mathrm{B}} T, \tag{5}$$

where $\boldsymbol{P}_i = \sum_j \boldsymbol{M}_{ij} \dot{\boldsymbol{U}}_j$, $\boldsymbol{K}_{ij} = [(\phi \boldsymbol{D}^{-1} \phi^t)^{-1}]_{ij}$ is the stiffness matrix for the CGP system, and $\boldsymbol{M}_{ij} = [(\phi \boldsymbol{m}^{-1} \phi^t)^{-1}]_{ij}$ is the mass matrix and $\boldsymbol{m} = m_\alpha \delta_{\alpha\beta}$. The displacements and momenta of CGPs are linearly related to those of the carbon atoms, but this relation is statistical so that it allows for a set of carbon atoms to explore widely the configuration sample space of the carbon atoms in proportion to the probability at the thermal equilibrium. The renormalized matrices $\boldsymbol{M}$ and $\boldsymbol{K}$ are nonlocal in i and j, and do not depend on the temperature because of the phonon approximation.

In the CGP method it is necessary to compute $\boldsymbol{D}^{-1}$, and a straightforward application of the CGP method to a system of a large number of atoms at once requires

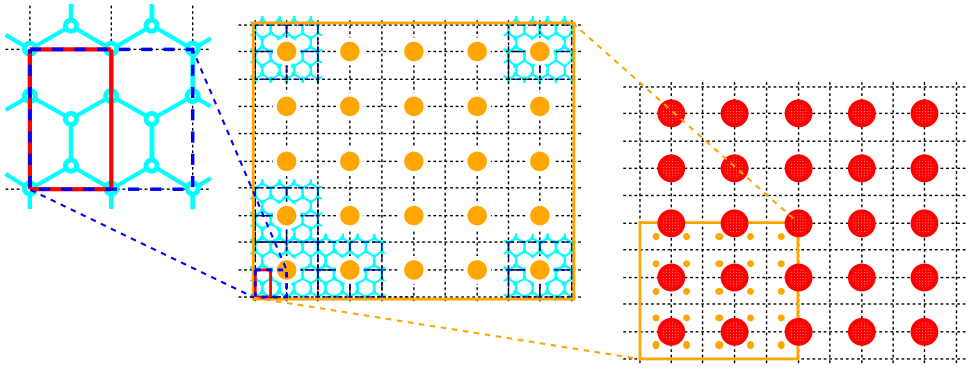

(a) (b) (c)

Figure 1: Generation of CGPs by the RCGP method from the carbon atoms of the graphene. (a) To choose a primitive cell (surrounded by red rectangular) from the carbon atoms in the honeycomb structure and to make a unit cell (surrounded by blue dashed rectangular) which contains 8 carbon atoms. (b) To expand the unit cell 10 times in both directions to yield a super cell (surrounded by orange rectangular) which contains 800 carbon atoms. The carbon atoms in the super cell are statistically projected onto 5×5 CGPs (particles in orange) which are set evenly. These are CGPs at the first stage. (c) To generate the second stage CGPs, a set of 25 CGPs at the first stage is expanded once in both directions so that $100 (= 4 \times 25)$ CGPs are generated and these are again statistically projected onto 5×5 CGPs which are the second stage CGPs. The process continues until the system size reaches the required length [Kobayashi, Nakamura, and Ogata (2008a)].

a large computational work and memories. In order to avoid these difficulties we apply the CGP method to a system with a relatively small number of atoms and expand the resulting system periodically in space, and recursively apply the CGP method to thus generated system until the system size becomes a desired scale. This method is similar to the renormalization group and called Recursive CGP method (RCGP method) [Kobayashi, Nakamura, and Ogata (2008a); Ogata, R. Kobayashi, and Gotoh (2009)].

The lattice system of CGPs can be chosen independent of that of the original atoms, an advantage that a relatively simple lattice structure can be used in the computation. Procedure of the RCGP method for the graphene proceeds as follows. Consider a primitive cell of carbon atoms within a red rectangular in Fig. 1(a) in which the relevant total number of atoms is counted as four. Then this primitive cell is expanded in the lateral direction once, so that the resulting cell (blue rectangular) is

a unit cell whose aspect ratio is $2:\sqrt{3}$ and contains 8 carbon atoms. The choice of the unit cell is not unique, and our criterion to choose this unit cell is to construct a rectangular as close to square as possible with a smaller number of carbon atoms. Now the unit cell is expanded 10 times in both lateral and vertical directions to yield a super cell (see Fig. 1(b)). The total number of carbon atoms included in this cell is $8\times10\times10=800$ and its domain size is $20\sqrt{3}d_C\times30d_C$, where d_C is the mean lattice distance of the carbons. These atoms are statistically projected onto 5×5 CGPs which are assumed to be put evenly in each direction within the domain under the periodic condition. These are the first stage CGPs. To generate the second stage CGPs, a set of 25 CGPs at the first stage is expanded once in both directions so that $100(=4\times25)$ CGPs are generated and these are again statistically projected onto 5×5 CGPs which are the second stage CGPs. By repeating the above RCGP process we can construct a CGP system whose spatial size is at the desired length. The CGP lattice at latter stage remains rectangular with the aspect ratio $2:\sqrt{3}$ by the construction.

The coarse graining in space must be accompanied by the coarse graining in time. Let $\lambda>1$ be a scale ratio of the coarse grained size in the RCGP process such that $\boldsymbol{R}^{(j+1)}=\lambda\boldsymbol{R}^{(j)}$ where $\boldsymbol{R}^{(j)}_{\alpha\beta}$ is the mean distance vector between CGPs α and β at j-th stage. A measure of the coarse graining in space is given by the ratio $\Lambda=\Delta x_{\mathrm{CG}}\,/\,\Delta x_{\mathrm{MD}}$, where Δx_{CG} and Δx_{MD} are the grid distances of CGPs at the final stage of the recursive coarse graining process and of the original atoms, respectively. Then the number of steps N_r necessary for the recursive process to attain Λ is determined by $N_r=\ln\Lambda/\ln\lambda$. The elastic moduli at j-th stage of the RCGP method is given by

$$\boldsymbol{C}^{(j)}=-\frac{1}{V_p}\sum_{\alpha,\beta}\boldsymbol{R}^{(j)}_{\alpha\beta}\boldsymbol{K}^{(j)}_{\alpha\beta}\boldsymbol{R}^{(j)}_{\alpha\beta}\,, \tag{6}$$

where V_p is the specific volume [Ashcroft and Mermin (1976)]. Since the magnitude of the elastic moduli should be unchanged under the coarse graining, i.e., $\boldsymbol{C}^{(j+1)}=\boldsymbol{C}^{(j)}$, we have $\boldsymbol{K}^{(j+1)}\propto\lambda^{d-2}K^{(j)}$, where d is the space dimension. The mass matrix scales as $\boldsymbol{M}^{(j+1)}=\lambda^d\boldsymbol{M}^{(j)}$, then the characteristic time of the CGP scales as $T^{(j+1)}\propto(||\boldsymbol{M}^{(j+1)}||/||\boldsymbol{K}^{(j+1)}||)^{1/2}\propto\lambda T^{(j)}$, which means $\Delta t_{\mathrm{CG}}\propto\lambda^{N_r}\Delta t_{\mathrm{MD}}=\Lambda\Delta t_{\mathrm{MD}}$ for the time increment in the computation, independent of the space dimension as far as the anharmonic effects are negligible.

Characteristics of the CGP method are

1. The CGP method introduces the weight function for the atoms, with which the positions of the atoms are thermally averaged following the statistical mechanics. Therefore the CGP method is relatively insensitive to the con-

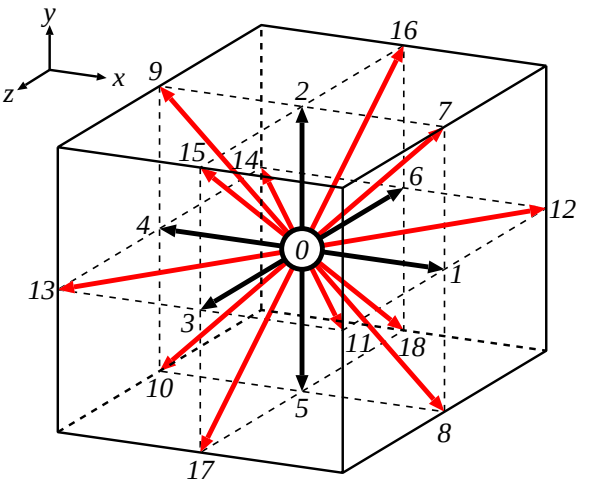

Figure 2: Fluid lattice and discrete velocities in D3Q19 model

figuration of the CGP's as compared to, e.g., the quasi-continuum method [Miller and Tadmor (2002)].

2. Degree of the coarse graining Λ can be tuned at any order. When Λ is unity, the CGP reduces to the original atom, thus the CGP method is transparent and suitable to develop a hybrid approach bridging over the different scales of motion.

3. Recursive use of the CGP method (RCGP method) makes it possible to connect the dynamics of atoms to that of the fluid motion with reasonable computational cost.

4. The RCGP has a freedom to choose a simpler grid system than that of the original system, which also reduces the computational work.

2.2 Lattice Boltzmann Method

Motion of the air is assumed to be described by the lattice Boltzmann equation. The lattice Boltzmann method (LBM) has recently been developed and found to be very effective for computation of various complex fluid motions. Advantage of LBM over the conventional fluid mechanics based on the Navier Stokes equation is that (1) the computational algorithm is so simple that actual implementation is easy, (2) all of the operations are local in physical space so that parallelization of computation is very efficient [Chen and Doolen (1998); Succi (2001); Sukop and Thorne Jr. (2006)].

In LBM, the fluid is represented by an ensemble of fluid particles which are assumed to exist only on grid points and allowed to move along the lines with small number of discrete directions $\alpha = 0, 1, \cdots, q-1$ and travel to the next grid point on a unit time Δt_{LB} with a prescribed velocity $\boldsymbol{c}_\alpha$ (see Fig. 2).

Let $f_\alpha(\boldsymbol{x},t)$ be a distribution function of the fluid particles traveling in the α-th direction. Then the macroscopic variables such as the fluid density ρ and the momentum $\rho\boldsymbol{v}$ are given by the 0th and 1st moment of the distribution function

$$\rho(\boldsymbol{x},t) = \sum_{\alpha=0}^{q-1} f_\alpha(\boldsymbol{x},t), \tag{7}$$

$$\rho(\boldsymbol{x},t)\boldsymbol{v}(\boldsymbol{x},t) = \sum_{\alpha=0}^{q-1} \boldsymbol{c}_\alpha f_\alpha(\boldsymbol{x},t). \tag{8}$$

The distribution function with q directions in d spatial dimensions is referred to as *DdQq* model. In this study we choose D3Q19 model (see Fig. 2). Evolution of the distribution function is given by

$$f_\alpha(\boldsymbol{x}+\boldsymbol{c}_\alpha dt, t+dt) - f_\alpha(\boldsymbol{x},t) = \Omega[f_\alpha(\boldsymbol{x},t)] \qquad (0 \leqq \alpha \leqq q-1) \tag{9}$$

The left hand side describes the translation and Ω is the collision operator for which we use the BGK approximation [Bhatnagar, Gross, and Krook (1954)]

$$\Omega = -\frac{1}{\phi}\left(f_\alpha(\boldsymbol{x},t) - f_\alpha^{\mathrm{eq}}(\rho(\boldsymbol{x},t), \boldsymbol{u}(\boldsymbol{x},t))\right), \tag{10}$$

where ϕ is a relaxation coefficient and f_α^{eq} is the local equilibrium distribution function given by

$$f_\alpha^{\mathrm{eq}} = \rho E_\alpha \left[1 + 3\boldsymbol{c}_\alpha \cdot \boldsymbol{v} + \frac{9}{2}(\boldsymbol{c}_\alpha \cdot \boldsymbol{v})^2 - \frac{3}{2}\boldsymbol{v}\cdot\boldsymbol{v}\right], \tag{11}$$

$$E_0 = 1/3, \quad E_1 = \cdots = E_6 = 1/18, \quad E_7 = \cdots = E_{18} = 1/36 \tag{12}$$

for D3Q19 model and is obtained by expanding the Maxwell Boltzmann distribution function up to the second order in the fluid velocity. It is well known that the Navier-Stokes equation is deduced from the lattice Boltzmann Eqs. (9) and (10) and by using the Chapman Enskog expansion. Then ϕ is related to the kinetic viscosity ν as

$$\nu = \frac{1}{3}\left(\phi - \frac{1}{2}\right). \tag{13}$$

The spatial accuracy of the LBM is the second order in the grid size.

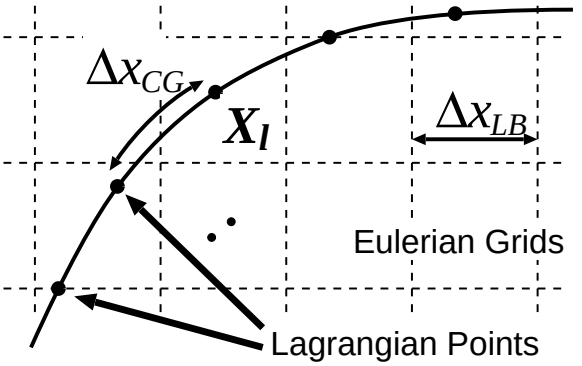

Figure 3: Eulerian grid points for LBM and Lagrangian points for the solid body in IBM.

2.3 Immersed boundary method

Since the time scales of the fluid and solid are widely separated (see Eq.(30)), the boundary condition at the interface should be the one such that it passes a reduced information of the fast variables of the solid phase to the slow variables of the fluid phase while assuring the momentum conservation between the two phases. By assuming that the fluid phase is continuum even at the scale of submicron meter, we choose the grid size of the fluid to be small enough to match with the mean separation distance of the CGP lattice at the final stage of the RCGP method, from which the degree of the coarse graining of the carbon atoms is fixed. Then the momentum exchanged at each time step of the CGP dynamics is accumulated during the one fluid time step and passed to the fluid motion. The details are as follows.

The macroscopic boundary condition for the fluid is assumed to be $\boldsymbol{v}(\boldsymbol{x}_B,t) = \boldsymbol{U}_B$ on the boundary where $\boldsymbol{x}_B$ and $\boldsymbol{U}_B$ are the position and velocity vectors of the boundary, respectively. In LBM, this is achieved by imposing the condition on the distribution function as

$$\tilde{f}_\beta(\boldsymbol{x}_B,t) = f_\alpha(\boldsymbol{x}_B,t) - 2\rho E_\alpha \frac{\boldsymbol{c}_\alpha \cdot \boldsymbol{U}_B}{c_s^2} \tag{14}$$

where $\tilde{f}_\beta$ is the distribution function just after the collision at the boundary, β is an index satisfying $\boldsymbol{c}_\beta = -\boldsymbol{c}_\alpha$ and E_α is given by Eq. (12) and c_s is the sound velocity $c_s^2 = c^2/3$ for D3Q19 model [Ladd (1994)]. When $\boldsymbol{U}_B = 0$, the above equation means the bounce back of fluid particle on the rest wall.

Since the graphene is represented by a set of CGPs in this study, it is natural and convenient to use IBM [Peskin (1977, 2003); Feng and Michaelides (2004); Niu,

Shu, Chew, and Peng (2006)]. In IBM, a solid body is regarded as an object which has a distributed force density on its surface so as to match the boundary condition at the body surface. Let $\boldsymbol{X}_l(\tau)$ be a position of l-th CGP on the surface which is not necessarily on the fluid grid point (see Fig. 3), where τ is the time variable in the CGP time scale. Suppose that the average distance between the nearest neighbor CGPs on the graphene surface is given by that of CGPs in the thermal equilibrium at the final stage of the recursive coarse graining process, i.e. $\Delta x_{\mathrm{CG}} = \Lambda \Delta x_{\mathrm{MD}}$. Then the degree of the coarse graining for the carbon atoms Λ is fixed by requiring

$$\Delta x_{\mathrm{LB}} = A_{\mathrm{L}} \Delta x_{\mathrm{CG}} = A_{\mathrm{L}} \Lambda \Delta x_{\mathrm{MD}}, \tag{15}$$

where A_{L} is a positive constant of order one. In other words, by this relation, the CGP spatial scale matches with that of LBE. Now consider the time scales. Because Λ is already determined by Eq.(15), we can estimate the time increment Δt_{CG} in the CGP computation by using $\Delta t_{\mathrm{CG}} = \Lambda \Delta t_{\mathrm{MD}}$ and the typical value of Δt_{MD} for the graphene carbon atoms. Since $A_{\mathrm{L}} \Delta x_{\mathrm{CG}} = \Delta x_{\mathrm{LB}} = c \Delta t_{\mathrm{LB}}$, we can fix Δx_{LB} with an appropriate value of A_{L}, say $A_{\mathrm{L}} = 1$, and we can determine the time increment Δt_{LB} by using the sound velocity c_s in the fluid and $c = \sqrt{3} c_s$. Then the ratio of the time increments is fixed as

$$\Delta t_{\mathrm{LB}} = A_{\mathrm{T}} \Delta t_{\mathrm{CG}}. \tag{16}$$

Generally A_{T} is large and about 150 in the present case of the air flow and the graphene (see Eq.(30)). This ratio means that one LBM computational cycle corresponds to A_{T} cycles in the CGP computation.

We use Eq.(14) at the CGP position $\boldsymbol{X}_l$ which generally does not coincide with the fluid grid point, therefore it is necessary to compute $f_\alpha(\boldsymbol{X}_l(\tau), t)$ from $f_\alpha(\boldsymbol{x}, t)$ at the fluid grid points by using the Lagrangian interpolation

$$f_\alpha(\boldsymbol{X}_l(\tau), t) = \sum_{i,j} \Psi(\boldsymbol{X}_l(\tau), \boldsymbol{r}_{ij}) f_\alpha(\boldsymbol{r}_{ij}, t), \tag{17}$$

where Ψ is the Lagrangian interpolation function and $\boldsymbol{r}_{ij}$ is the position vector of the fluid grid point near $\boldsymbol{X}_l(\tau)$. Note that the time variable t of f_α is unchanged, which means that the distribution function is assumed to be still because the distribution function is a slow variable and only the CGP position $\boldsymbol{X}_l(\tau)$ changes rapidly in the LB time unit. We assume that the fluid particles undergo the elastic collision at the solid surface and that Eq.(14) holds even at time scale of $\Delta t_{\mathrm{CG}} = \Delta t_{\mathrm{LB}} / A_{\mathrm{T}}$. In the following discussion in this section, we use the notation $d\tau = \Delta t_{\mathrm{CG}}$ for convenience. Collisions of the fluid particles with one CGP during time interval $d\tau$ yields the change in the distribution function

$$\delta f_\beta(\boldsymbol{X}_l(\tau), t)\, d\tau = [\tilde{f}_\beta(\boldsymbol{X}_l(\tau), t) - f_\alpha(\boldsymbol{X}_l(\tau), t)]\, d\tau\,. \tag{18}$$

Then the momentum change that the fluid receives is

$$\boldsymbol{g}(X_l(\tau),t)\ \delta\boldsymbol{A}_{\mathrm{L}}\ d\tau = \sum_{\beta} \boldsymbol{c}_\beta \cdot \delta f_\beta(\boldsymbol{X}_l(\tau),t)\ \delta\boldsymbol{A}_{\mathrm{L}}\ d\tau\ , \tag{19}$$

where $\delta\boldsymbol{A}_{\mathrm{L}}$ is the surface element at $\boldsymbol{X}_l(\tau)$ and $\boldsymbol{g}$ is the impulse density. The reaction force on the CGP on the surface is given by $-\boldsymbol{g}\delta\boldsymbol{A}_{\mathrm{L}}d\tau$, so that the dynamical equation of the CGP is symbolically written as

$$\frac{d\boldsymbol{P}_l(\tau)}{d\tau} = -\frac{\partial H_{CG}}{\partial \boldsymbol{X}_l} - \boldsymbol{g}_l(\tau)\ \delta\boldsymbol{A}_{\mathrm{L}}\ . \tag{20}$$

On the other hand, since the force density $\boldsymbol{g}(\boldsymbol{X}_l,t)d\tau$ is distributed on the body surface, the force acting on the fluid at $\boldsymbol{X}_l$ must be redistributed on the fluid grid points by the linear rule

$$\tilde{\boldsymbol{F}}(\boldsymbol{x},t+\tau)\ d\tau = \sum_{l} \boldsymbol{g}(\boldsymbol{X}_l(\tau),t) D(\boldsymbol{x}-\boldsymbol{X}_l(\tau))\ \delta\boldsymbol{A}_{\mathrm{L}}\ d\tau\ , \tag{21}$$

where D is given by

$$D(\boldsymbol{x}-\boldsymbol{X}_l) = \prod_{\alpha}^{d} \delta_h\left(x_\alpha - (\boldsymbol{X}_l)_\alpha\right)\ , \tag{22}$$

$$\delta_h(x) = \begin{cases} \frac{1}{2h}(1+\cos(\frac{\pi x}{h})) & |x| \le h \\ 0 & \text{otherwise} \end{cases} \tag{23}$$

with the grid spacing $h = 2\Delta x_{\mathrm{LB}}$ [Niu, Shu, Chew, and Peng (2006)]. Finally the force acting on the fluid during the time interval Δt_{LB} is given by accumulating the small impulses $\tilde{\boldsymbol{F}}(\boldsymbol{x},t+\tau)d\tau$

$$\boldsymbol{F}_{\mathrm{ext}}(\boldsymbol{x},t) = \int_0^{A_{\mathrm{T}}\Delta t_{CG}} \tilde{\boldsymbol{F}}(\boldsymbol{x},t+\tau)\ d\tau. \tag{24}$$

When the external force is applied to the fluid, the fluid velocity is changed as

$$\boldsymbol{v}(\boldsymbol{x},t+\Delta t_{\mathrm{LB}}) = \boldsymbol{v}(\boldsymbol{x},t) + \frac{\Delta t_{\mathrm{LB}}\boldsymbol{F}_{\mathrm{ext}}(\boldsymbol{x},t)}{\rho(\boldsymbol{x},t)} \tag{25}$$

which appears in the velocity field in f_α^{eq}. In the computation of LBE, we use the following formula with the enhanced numerical stability in the nondimensional form [Buick and Greated (2000)]

$$\begin{aligned} f_\alpha(\boldsymbol{x}+\boldsymbol{c}_\alpha,t+1) - f_\alpha(\boldsymbol{x},t) = \\ -\frac{1}{\phi}\left(f_\alpha(\boldsymbol{x},t) - f_\alpha^{\mathrm{eq}}\left(\rho,\boldsymbol{u}-\frac{\boldsymbol{F}_{\mathrm{ext}}}{2\rho}\right)\right) - \left(\frac{2\phi-1}{2\phi}\right)\frac{3}{2}E_\alpha\boldsymbol{c}_\alpha\cdot\boldsymbol{F}_{\mathrm{ext}}. \end{aligned} \tag{26}$$

Table 1: Characteristic values

Atomic length	$\tilde{l}_{\mathrm{AU}} = 5.3 \times 10^{-11}$ [m]
Atomic time	$\tilde{t}_{\mathrm{AU}} = 2.4 \times 10^{-17}$ [s]
Atomic mass	$\tilde{m}_{\mathrm{AU}} = 9.1^{-31}$ [kg]
Atomic velocity	$\tilde{u}_{\mathrm{AU}} = \tilde{l}_{\mathrm{AU}}/\tilde{t}_{\mathrm{AU}} = 2.2 \times 10^{6}$ [m/s]
Loschmidt constant	$n_0 = 2.687 \times 10^{25}$ [1/m^3]
Molecular mass (air)	$m_{\mathrm{air}} = 4.851 \times 10^{-26}$ [kg]
Sound velocity	$\tilde{c}_s = 3.315 \times 10^{2}$ [m/s]
Grid distance	$\Delta\tilde{x}_{\mathrm{LB}} = \Delta\tilde{x}_{\mathrm{CG}} = 0.2561 \times^{-6}$ [m]
Time increment in CGP	$\Delta\tilde{t}_{\mathrm{CG}} = 2.9734822 \times 10^{-12}$ [s]
Time increment in LB	$\Delta\tilde{t}_{\mathrm{LB}} = A_{\mathrm{T}}\Delta\tilde{t}_{\mathrm{CG}} = 0.44602233 \times 10^{-9}[s] = 0.446$[ns]
Force unit in LB	$\tilde{F}_{\mathrm{LB}} = 3n_0 m_{\mathrm{air}}\tilde{c}_s^2\Delta\tilde{x}_{\mathrm{LB}}^2 = 2.8184 \times 10^{-8}$ [N]

2.4 Force and velocity units

It is important and necessary for theoretical consideration and numerical computation to examine the relation between the units used in the dynamics of CGPs and the fluid. In the molecular dynamics of the solid phase, the Hartree atomic units is commonly used and we also use it for the CGP dynamics. In the fluid, the length and velocity are nondimensionalized in terms of $\Delta\tilde{x}_{\mathrm{LB}}$ and $\tilde{c} = \sqrt{3}\tilde{c}_s$, respectively, where quantities with ˜ are those with dimensions. When the unit is switched from one phase to the other, the following nondimensional coefficients are necessary :

$$B_{\mathrm{V}} = \frac{\tilde{u}_{\mathrm{AU}}}{\sqrt{3}\tilde{c}_s}, \qquad B_{\mathrm{F}} = \frac{\tilde{F}_{\mathrm{CG}}}{\tilde{F}_{\mathrm{LB}}}, \tag{27}$$

where

$$\tilde{F}_{\mathrm{LB}} = \frac{\rho_0\tilde{c}(\Delta\tilde{x}_{\mathrm{LB}})^d}{\Delta\tilde{t}_{\mathrm{LB}}} = \rho_0\tilde{c}^2(\Delta\tilde{x}_{\mathrm{LB}})^{d-1} = n_0 m_{\mathrm{air}}\left(\sqrt{3}\tilde{c}_s\right)^2(\Delta\tilde{x}_{\mathrm{LB}})^{d-1} \tag{28}$$

$$\tilde{F}_{\mathrm{CG}} = \tilde{m}_{AU}\tilde{u}_{AU}^2/\tilde{l}_{AU}. \tag{29}$$

When we take $A_{\mathrm{L}} = 1$, $\Lambda = 1024$ and the values in Tab. 1, we have

$$A_{\mathrm{L}} = \Delta x_{\mathrm{LB}}/\Delta x_{\mathrm{CG}} = 1, \qquad A_{\mathrm{T}} = \Delta t_{\mathrm{LB}}/\Delta t_{\mathrm{CG}} = 150. \tag{30}$$

Then the coefficients for the present case are

$$B_{\mathrm{V}} = 3.810 \times 10^{3}, \quad B_{\mathrm{F}} = 2.923\ . \tag{31}$$

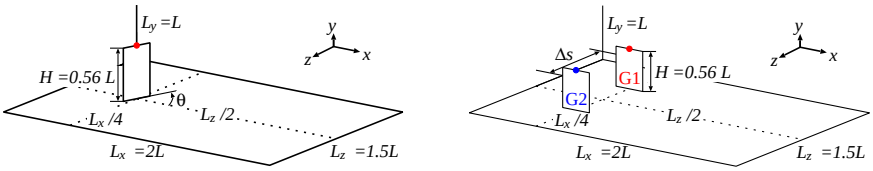

(a) (b)

Figure 4: Configuration of the graphenes in the flow. (a) Single graphene with the angle of attack θ, (b) A pair of graphenes G1 and G2 with separation distance Δs. Points on the top edge of each graphene are the CGPs used to measure the displacement due to the graphene vibration.

These values are used to convert the velocity and force in the CGP unit to those in the LB unit as

$$\boldsymbol{v}_{\mathrm{LB}} = B_{\mathrm{V}}\boldsymbol{v}_{\mathrm{CG}}, \qquad \boldsymbol{F}_{\mathrm{LB}} = B_{\mathrm{F}}\boldsymbol{F}_{\mathrm{CG}}. \tag{32}$$

3 Results

3.1 Single graphene in laminar flow

We have applied the hybrid computational method described in the previous section to the problems of the interaction between the graphene and the air flow. First we consider the motion of a single graphene in a laminar flow. The graphene is fixed perpendicularly at the bottom plate (see Fig. 4(a)). Incoming flow is assumed to be steady Blasius type flow for which the fluid velocity is zero at the bottom and gradually increases and becomes uniform at far distance ($y > 0.1H$). The flow field is divided into $120 \times 60 \times 90$ cubes in x, y, and z directions, respectively. The Reynolds number is defined as $Re = U_{\max}H/\nu$, where $U_{\max}$ is the maximum speed at the entrance, H the height of the graphene, and ν the kinematic viscosity. The Reynolds number is controlled by $U_{\max}$ and the four cases of $Re = 1, 10, 20$ and 40 are examined which correspond to $U_{\max}/c = 0.00260, 0.0260, 0.0519, 0.104$, respectively. The graphene is composed of 5×40 CGPs, and one CGP represents 2×10^6 carbon atoms, so that the graphene sheet size is 1.2 [μm] in width (W), and 8.8 [μm] in height (H). The angle of attack to the flow is $\theta = 0^\circ, 30^\circ, 60^\circ, 90^\circ$.

In order to obtain a well posed initial flow field, the LB equation is integrated for 15000 steps (which corresponds to the time that the mean flow passes through the whole domain about 7.5 times when $Re = 40$) to attain a steady state of the flow during which the graphene is sustained to be rigid. After this time the graphene is

released to freely move under the action of the flow field.

We examine how the graphene responds to the flow. For this purpose, the time variation of the displacement of CGP at the middle position of the top edge of the graphene as marked by red (and blue for a pair of graphenes) point in Fig. 4 (a) is shown in Fig. 5 for various Reynolds numbers at $\theta = 90^\circ$. It is seen that immediately after the release (at $t_0 = 6.7$ [μs]) the graphene begins to bend downstream with oscillation and attains certain equilibrium state. The graphene bends deeply with increase of the Reynolds numbers and its oscillation frequency is not equal but very close to the eigen frequency of the graphene. The eigen frequency of the graphene was computed by simulating the perturbed CGP graphene in the absent of fluid. Approach to the equilibrium position is faster for the higher Reynolds numbers.

Fig. 6 shows the temporal evolution of the drag and lift coefficients defined by

$$C_{\mathrm{D}} = \frac{F_{\mathrm{D}}}{\rho_f U_b^2 A/2}, \quad C_{\mathrm{L}} = \frac{F_{\mathrm{L}}}{\rho_f U_b^2 A/2}, \tag{33}$$

where F_{D} and F_{L} denote the drag and lift forces acting on the graphene, respectively, ρ_f is the fluid density, and A is the area of the graphene WH. U_b is the volume-averaged stream wise velocity defined by

$$U_b(t) = \frac{1}{V} \iiint U(x,y,z,t)\, dxdydz, \tag{34}$$

where V is the total volume of the computational domain of the flow. The drag coefficient is larger by one order than the lift coefficient. Both coefficients become smaller with increase of the Reynolds numbers, which is consistent with the general trend of decrease of C_D for low Reynolds numbers at macro scale flow, for example $C_D = 24/Re$ for the sphere [Batchelor (1967)].

Consider now the effects of the angle of attack on the graphene motion. Fig. 7 shows the time variation of the displacement of the marked CGP at the top edge of the graphene for four angles of attack at $Re = 40$. For $\theta = 30^\circ$ the oscillation of the graphene grows in time without bound, while for $\theta \geq 60^\circ$ it decays. When $0^\circ < \theta < 90^\circ$, the symmetry of the flow field is broken and the lift force is generated. Although the drag force dominates the lift force, the oscillation amplitude in both forces are growing in time when $\theta = 30^\circ$. On the other hand, when $\theta = 60^\circ$ the oscillation in the drag and lift forces vanishes. It is worth while to note that the fluttering of the graphene sheet at moderate angles of attack and its suppression at large angles of attack are observed also for a wing in the high speed flow at ordinary macroscopic scale [Tang and Dowell (2001); Hashimoto, Furuta, Yagi, and Nakamura (2007)].

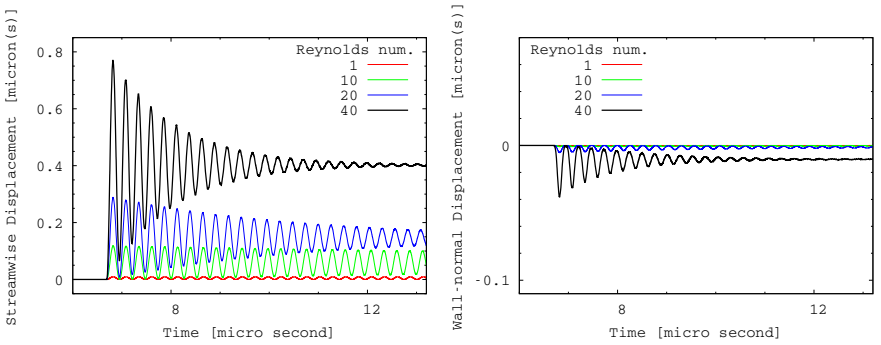

(a) (b)

Figure 5: Time series of displacement of the marked CGPs of the graphene at $\theta = 90^\circ$ for $Re = 1, 10, 20, 40$. Release time is at $t_0 = 6.7$ [μs]. (a) stream wise direction, (b) direction normal to the bottom plate.

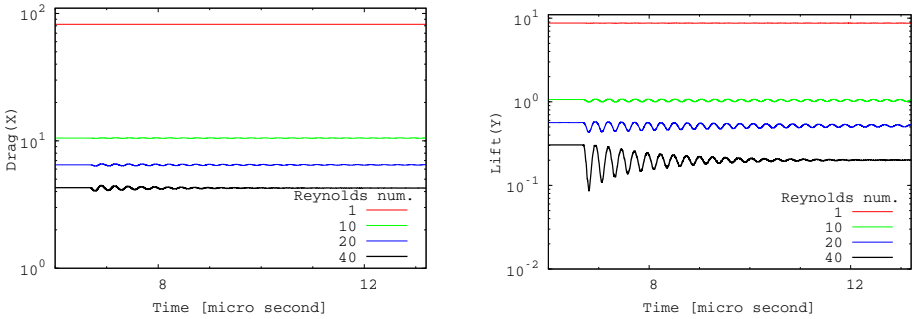

(a) (b)

Figure 6: Time series of the drag and lift coefficients of the graphene at $\theta = 90^\circ$ for $Re = 1, 10, 20, 40$. Release time is at $t_0 = 6.7$ [μs]. (a) drag coefficient, (b) lift coefficient.

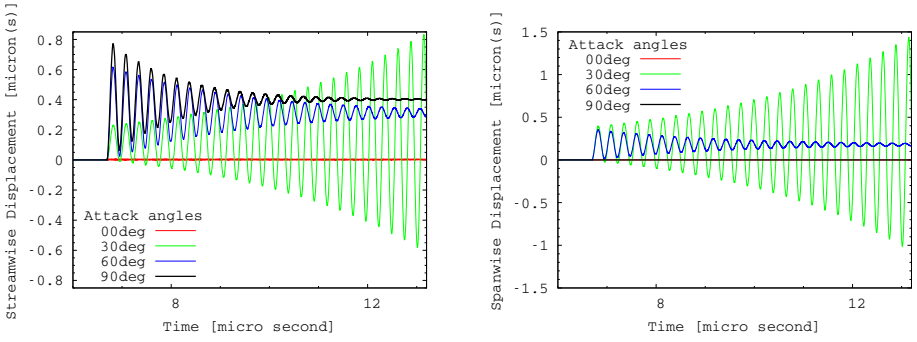

(a) (b)

Figure 7: Time series of the displacement of the marked CGP. Release time is at $t_0 = 6.7$ [μs] (a) stream wise direction, (b) span wise direction. For $\theta = 0^\circ, 30^\circ, 45^\circ, 60^\circ, 90^\circ$ at $Re = 40$.

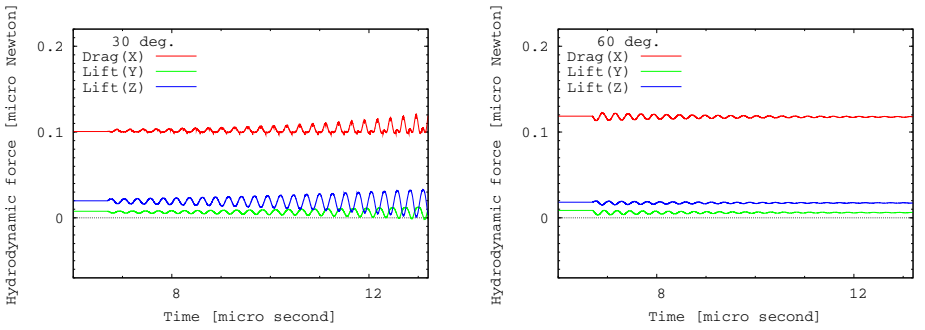

(a) (b)

Figure 8: Time series of the forces acting on the graphene at $Re = 40$. Release time is at $t_0 = 6.7$ [μs]. (a) $\theta = 30°$, (b) $\theta = 60°$.

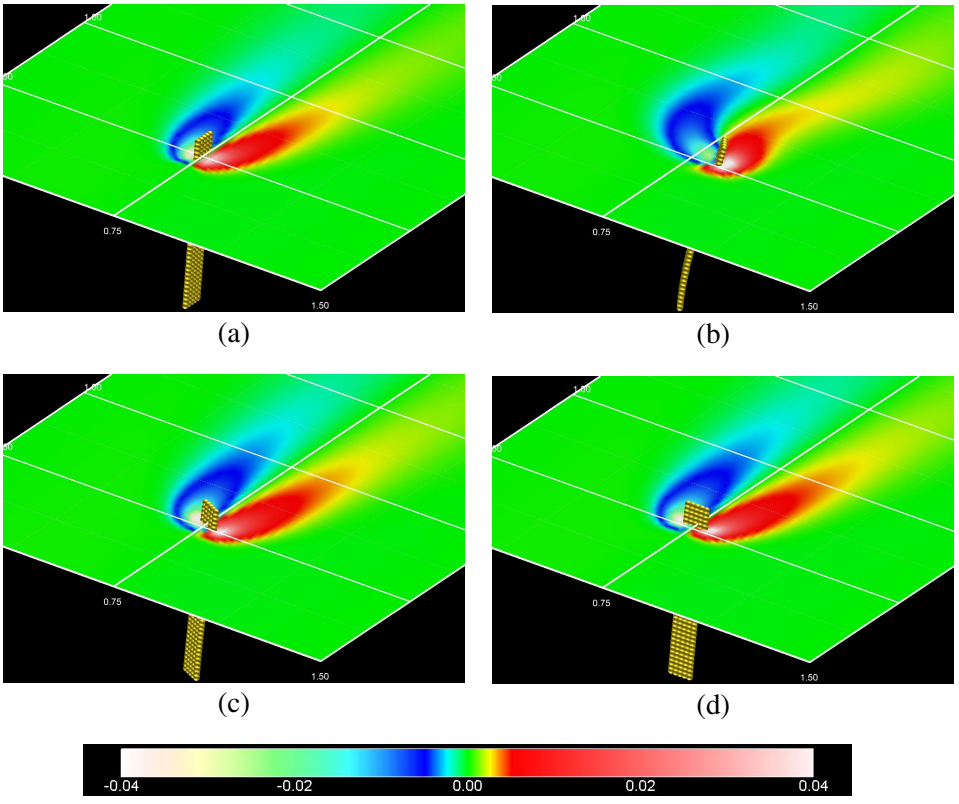

(a) (b) (c) (d)

Figure 9: Single graphene with the angle of attack to the mean flow and the y component of the vorticity on the plane at $y/L = 1/2$ at $Re = 40$ and $t = 13.4$ [μs]. Particles show positions of CGPs (the particle size does not indicate the CGP size) and color represents the vorticity amplitudes. (a) $\theta = 0°$, (b) $\theta = 30°$, (c) $\theta = 60°$, (d) $\theta = 90°$.

Fig. 9 shows the graphene and the y component of the vorticity on the plane at $y = L/2$ at $t = 13.4$ [μs] for four angles of attack $\theta = 0^\circ, 30^\circ, 60^\circ, 90^\circ$ and for $Re = 40$. The vorticity is concentrated near the edge of the graphene. When $\theta = 30^\circ$ and 60°, the vorticity is distributed asymmetry and the graphene sheet is very weakly twisted.

3.2 A pair of graphenes in laminar flow

We now consider the motion of a pair of graphenes which are set in parallel to the flow and fixed to the bottom plate with distance Δs (see Fig. 4(b)). The numerical parameters, the initial and boundary conditions of the flow are mostly the same as those in the case of the single graphene. Five cases of spacings $\Delta s = 1.02, 2.05, 4.10, 8.20$, and 11.5 [μm] are examined. For $\Delta s = 1.02$, 2.05 and 11.5 [μm], the total time of integration is 30000 time steps in the LB unit which correspond to 13.4 [μs], and 60000 time steps corresponding to 26.8 [μs] for $\Delta s = 4.10$ and 8.20 [μm].

Unlike the case of the single graphene with the angle of attack $\theta = 0^\circ$, the pair of graphenes begins to oscillate after release, irrespective of the Reynolds numbers, and the oscillation amplitude becomes larger with the Reynolds numbers (figure not shown). For $Re = 40$ the pair of graphenes collide each other at latter times. In order to prohibit crossing of the graphenes we introduce a repulsive force in terms of the Lennard-Jones type potential between the sheets,

$$\boldsymbol{F}_{i,\mathrm{Rep}}(r) = \begin{cases} \frac{4\varepsilon}{\Delta x_{\mathrm{CG}}} \sum_j \left\{ 12 \left(\frac{\Delta x_{\mathrm{CG}}}{r_{ij}} \right)^{13} - 6 \left(\frac{\Delta x_{\mathrm{CG}}}{r_{ij}} \right)^{7} \right\} \frac{\boldsymbol{r}_{ij}}{r_{ij}}, & \text{for} \quad r_{ij} < \Delta x_{\mathrm{CG}} \\ 0 & \text{for} \quad r_{ij} \geq \Delta x_{\mathrm{CG}} \end{cases} \tag{35}$$

with $\varepsilon = 1000$[eV], where r_{ij} is the distance between two CGPs each of which is on the different graphene sheet, respectively.

Fig. 10 shows the temporal evolution of the displacement of the marked CGPs on each top edge of the graphenes for five separation distance at $Re = 40$. Note that $t = 0$ corresponds to the time at which the graphenes are released. After the release the oscillation amplitudes grow to collide each other irrespective of the separation distance. When $\Delta s \leq 2.05$ [μm], the oscillation is periodic even when they are colliding, but when $\Delta s \geq 4.10$ [μm], the oscillation becomes chaotic at large times. This may be compared with the case of a pair of flexible filaments in a flowing soap film in which two modes of parallel flapping and mirror-image clapping are observed depending on the separation distance between the two filaments [Zhang, Childress, Libchaber, and Shelley (2000); Zhu and Peskin (2003)]. When $\Delta s = 11.5$ [μm], the graphene configuration becomes identical to the periodic array of the graphenes with the same distance with the zero angle of attack, so that no oscillation

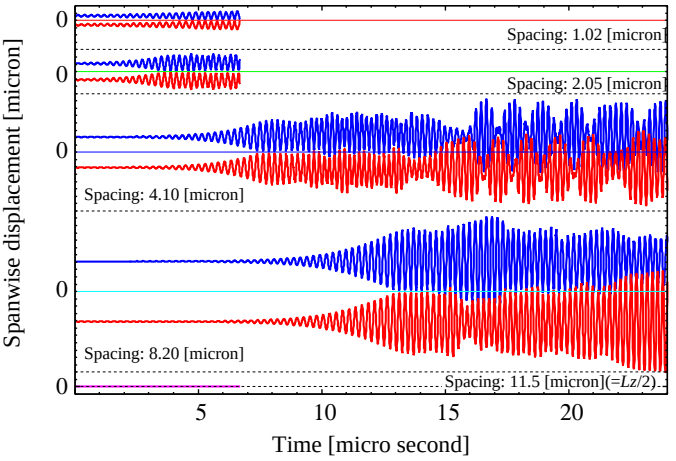

Figure 10: Time series of the displacements of the marked CGPs at the top edge of the graphenes after release for five separation distances at $Re = 40$. Red : G1, blue : G2 in Fig. 4.

occurs by the symmetry. The curves at large times for $\Delta s \geq 4.10$ [μm] look to cross, but this is not the case. Because one graphene is above the other one as seen in Fig. 11 in which the strain amplitudes are shown in color at the position of CGPs for $\Delta s = 8.20[\mu\text{m}]$ at three times $t = 13.8, 15.6$, and 22.7 [μs] after release for $Re = 40$. The figures show that at the initial phase two graphenes vibrate in a symmetric way, but as time goes on they begin to collide each other so that the graphene sheets are vibrating, hitting and even twisting very chaotically.

Flow field is also responding to the chaotic vibration of the graphenes and exhibits complex pattern. Figure12 shows the distribution of y component of the vorticity on the plane at $y = L/3$ at the same time as those of Fig. 11 for $\Delta s = 8.20[\mu\text{m}]$ for $Re = 40$. It can be seen that the vorticity is large near the graphenes, and each graphene is accompanied by a pair of positive and negative vorticity in the y component. Regions with moderate amplitudes of the vorticity extend in the direction perpendicular to the mean flow, which is due to the rapid vibrating motion of the graphenes in that direction.

As a result of complex interaction between the graphenes and the air flow the forces acting on the graphenes become chaotic. Figure13 shows the temporal evolution of the nondimensionalized drag and lift forces acting on the blue-colored graphene G2 in Fig. 4(b). It is observed that when the separation distance increases the mean values become smaller but the fluctuations become larger and chaotic at latter times.

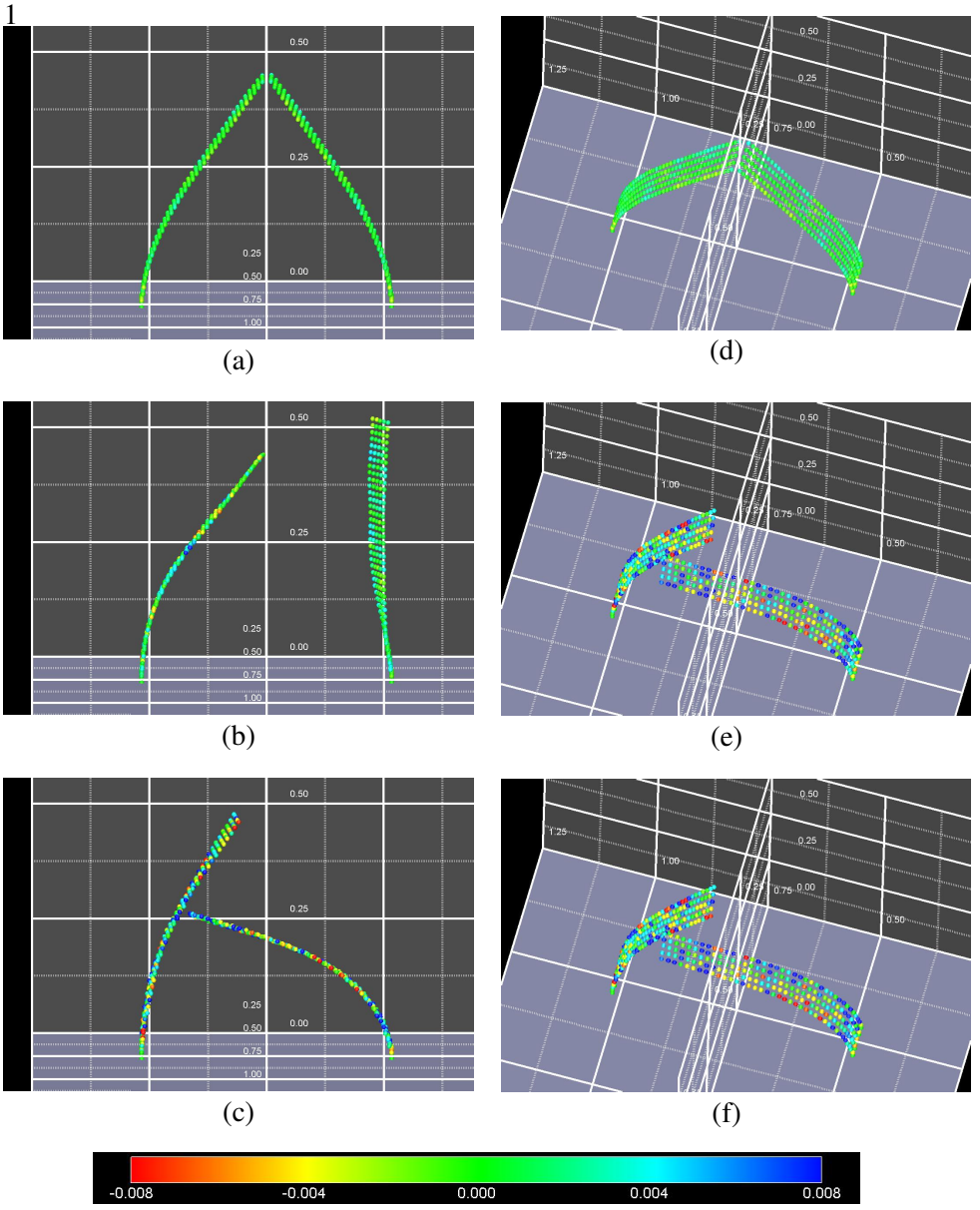

Figure 11: Vibration of a pair of graphenes and the strain distribution for $\Delta s = 8.2$ [μm] at $Re = 40$. Particles show positions of CGPs (particle size does not indicate the CGP size) and color represents the strain amplitude. Red : compressed region, blue: stretched region. View from downstream at (a) $t = 13.8$ [μs], (b) $t = 15.6$ [μs], and (c) $t = 22.7$ [μs], and bird's eyes view at (d) $t = 13.8$ [μs], (e) $t = 15.6$ [μs], and (f) $t = 22.7$ [μs] after release.

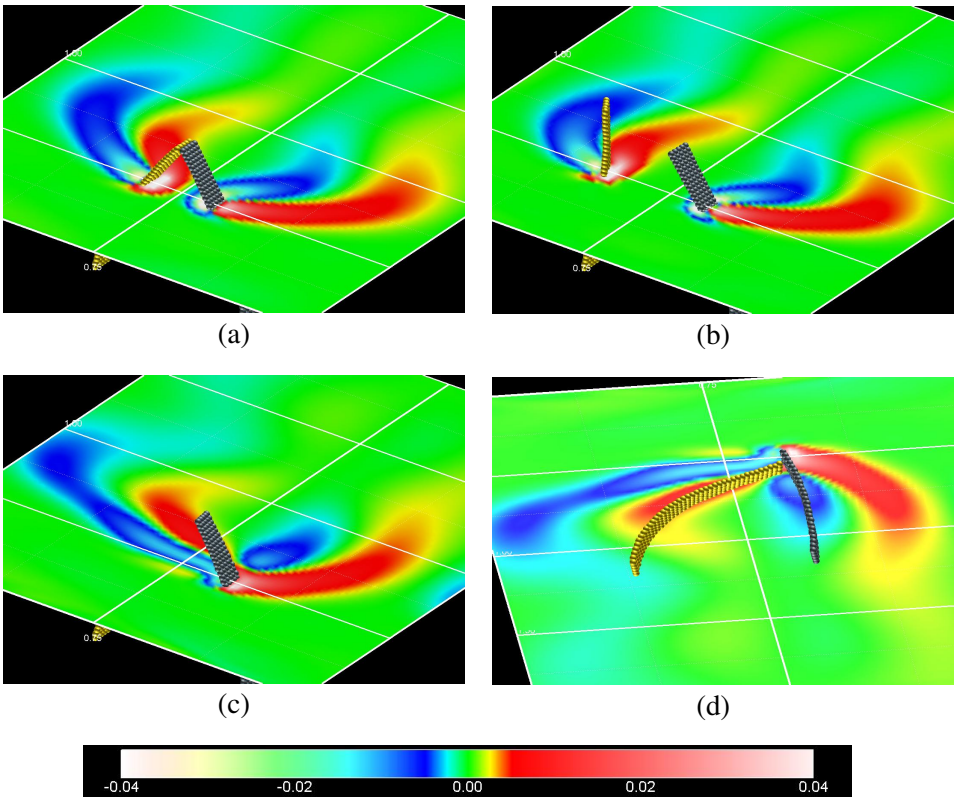

Figure 12: A pair of graphenes and the y component of the vorticity on the plane at $y/L = 1/3$ for $\Delta s = 8.2$ [μm] at $Re = 40$. Particles show positions of CGPs (particle size does not indicate the CGP size) and color represents the vorticity amplitudes. (a) $t = 13.8$ [μs], (b) $t = 15.6$ [μs], and (c) $t = 22.7$ [μs], and (d) view from the bottom plate at $t = 22.7$ [μs] after release.

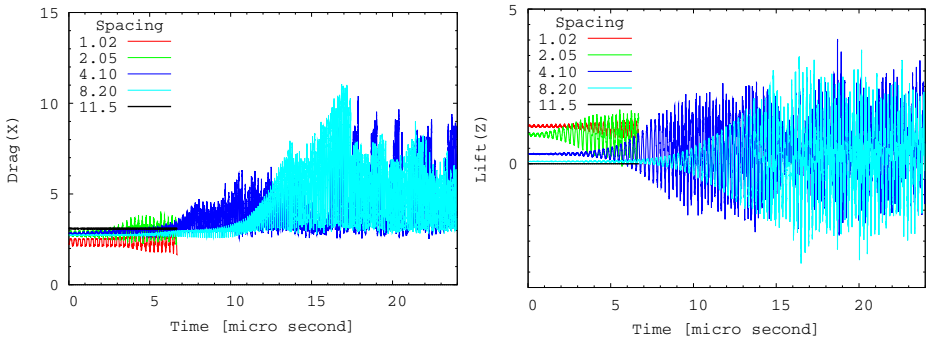

Figure 13: Time series of the nondimensional forces acting on the graphene after release for $Re = 40$. (a) stream wise direction, (b) span wise direction.

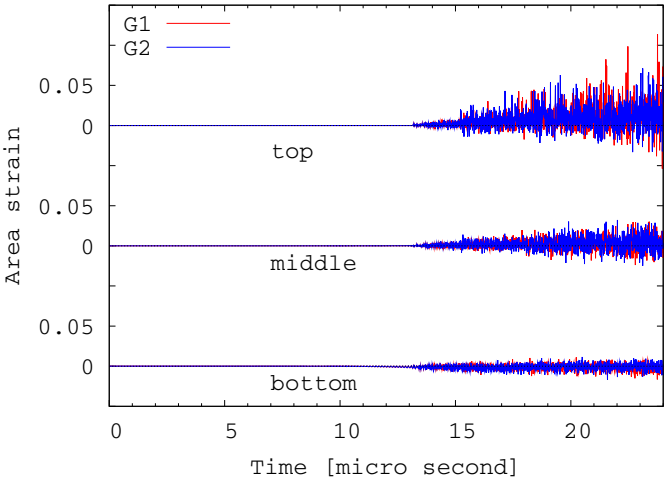

Figure 14: Time series of the area strain ε_l at the bottom, middle and top on the leading edge of the graphenes after release for $Re = 40$. Red: G1, blue : G2.

Since the graphenes are deformed due to the hydrodynamics forces, the stress distribution is generated inside the graphenes. The stress is proportional to the rate of change in the area of the local surface element at l-th CGP position which is quantified as area strain by $\varepsilon_l = (|\delta \boldsymbol{A}_l| - |\delta \boldsymbol{A}_{l0}|)/|\delta \boldsymbol{A}_{l0}|$ where $|\delta \boldsymbol{A}_{l0}|$ is the area of the surface element at the equilibrium, so that the distribution of the strain field can be visualized by ε_l. The strain distribution inside the graphenes at several times is shown by color in Fig. 11. When the vibration amplitudes of the graphene pair are small, the strain fluctuations are small, but when the collision begins strong strain waves accompanied with large fluctuations are excited.

It would be physically plausible that when the graphenes are fixed on the flat bottom plate with the GaN-AlGaN junction at a few nanometers below the surface the strain at the bottom of the graphene would change the electron distribution at the junction. This implies a possibility to develop a flow sensor by measuring the electron current. Such a composite structure will be realized by further advancing the fabrication technique for the composite structure of graphenes and carbon nanotubes [Kondo, Sato, and Awano (2008)]. In this connection we here note that a micro-cantilever of piezoelectric material fabricated on a silicon-on-insulator wafer has already been proposed as a sensitive flow sensor [Kaabi, Kaabi, Sakly, and AbdelMalek (2007); Zhang, Ruan, Wang, Zhou, Wang, and Liu (2010)]. To see this,

we show in Fig. 14 the time evolution of the strain measured at bottom, middle and top of the leading edges of two graphenes. Each signal becomes chaotic at about $t = 12$ [μs] and the strain at the top has the largest amplitudes, which is probably due to the collision effects. In fact, at early phase before collision, it is observed that the strain at the bottom of the graphene is the largest although the amplitude is very small.

4 Summary and discussions

We have developed the hybrid computational method to numerically simulate the interaction between the graphenes and the air flow from the microscopic description of the graphene carbon atoms, which is a typical multi-scale multi-physics problem. In order to match the spatial and time scales of the two different dynamics at the boundary, three step coarse graining strategy was used. The first step was done by deducing the CGP Hamiltonian from that of the carbon atoms of the graphene under the phonon approximation. The second step was to repeat the first procedure recursively to attain a certain length scale at which the lattice size of the CGP system is comparable to the smallest fluid grid size. In the first and second steps (RCGP method) both length and time of the CGP dynamics are scaled in the same way, but there still exists a gap in time scale. The air flow motion was described by the LB equation and the momentum exchange at the boundary was treated by IBM. The third step was to accumulate a number of small impulses acting on the fluid over the LB time interval.

The numerical computation of the air flow and CGPs with the coarse grained boundary condition, the hybrid computational method, was used to analyze the motion of a single graphene and a pair of graphenes in the steady flow. It was found that the single graphene with the angles of attack 60° and 90° to the flow direction begins to bend downstream with oscillation after release and tends to attain the equilibrium form, but the oscillation amplitudes for the angle of attack 30° increases in time. Also found was that when the separation distance of a pair of graphenes is large, the oscillation amplitudes become larger and chaotic, and they collide each other. The oscillation frequency was very close but not equal to that of the eigen frequency of the single graphene in the absent of fluid. The vibration pattern of a pair of graphene becomes quite complicated when the separation becomes larger. The strain distribution inside the graphene was also computed by the present method. It was observed that when the collision occurs the strong strain waves accompanied with large fluctuations are excited. It was argued that this strain field information can be used to develop a fluid sensor or fluid driver [Kaabi, Kaabi, Sakly, and AbdelMalek (2007); Zhang, Ruan, Wang, Zhou, Wang, and Liu (2010)].

Although the results by the present hybrid computational method are encouraging,

there remain points to be carefully examined. First consider accuracy. Error in the diagonal components of the macroscopic elastic constants computed by the RCGP method is known to be less than 10% [Inoue, Tanaka, Kobayashi, Ogata, and Gotoh (2008)] and the error in the drag coefficient by IBM is about 5-10% in the context of usual fluid mechanics at macro scales, irrespective of using LBE or the Navier-Stokes equation. Currently we are examining the same problem but with the Navier-Stokes equation instead of LBE and the preliminary results are quite promising for the present approach in the accuracy and computational costs, which will be reported elsewhere. Second, the boundary condition needs more careful treatment. We have used the bounce back boundary condition Eq.(14) for the distribution function of LBM at the interface. Underlying assumption is that the solid phase is a wall with large mass density when compared to that of fluid. In other words, no mass density ratio, say $\zeta = \rho_{\text{fluid}}/\rho_{\text{solid}}$, appears in the equation, and the reflection coefficient as a macroscopic parameter for intermolecular force should also be considered. It is necessary for more accurate computation of the fluid-solid interaction to study these effects theoretically and numerically with the help of the molecular dynamics. The hybrid computation which takes into account those effects is a real challenge to the multi-scale multi-physics simulation.

Acknowledgement: This work was supported by the Japan Science and Technology Agency. The authors thank the Information Technology Center at Nagoya University for the computational support.

References

Ashcroft, N.; Mermin, N. (1976): *Solid state physics*. HRW Int'l ed. (Saunders College, Philadelphia).

Batchelor, G. (1967): *An introduction to fluid mechanics*. Cambridge University Press Cambridge.

Benvenuto, A.; Guarnieri, V.; Lorenzelli, L.; Collini, C.; Decarli, M.; Adami, A.; Potrich, C. Lunelli, L.; Canteri, R.; Pederzolli, C. (2008): Fabrication of a MEMS-based separation module for liquid chromatography. *Sensors and Actuators B: Chemical*, vol. 130, pp. 181–186.

Bhatnagar, P.; Gross, E.; Krook, M. (1954): A model for collision processes in gases. I. Small amplitude processes in charged and neutral one-component systems. *Physical Review*, vol. 94, no. 3, pp. 511–525.

Buick, J.; Greated, C. (2000): Gravity in a lattice Boltzmann model. *Physical Review E*, vol. 61, no. 5, pp. 5307–5320.

Chen, S.; Doolen, G. (1998): Lattice Boltzmann method for fluid flows. *Annual Review of Fluid Mechanics*, vol. 30, no. 1, pp. 329–364.

Feng, Z.; Michaelides, E. (2004): The immersed boundary-lattice Boltzmann method for solving fluid–particles interaction problems. *Journal of Computational Physics*, vol. 195, no. 2, pp. 602–628.

Hashimoto, A.; Furuta, Y.; Yagi, N.; Nakamura, Y. (2007): Analysis of a fluttering delta wing with large deformation at low subsonic speeds. *Journal of the Japan Society for Aeronautical and Space Sciences*, vol. 55, pp. 104–110.

Inoue, Y.; Tanaka, J.; Kobayashi, R.; Ogata, S.; Gotoh, T. (2008): Multiscale numerical simulation of fluid-solid interaction. *Materials Transactions*, vol. 49, no. 11, pp. 2550–2558.

Kaabi, L.; Kaabi, A.; Sakly, J.; AbdelMalek, F. (2007): Modelling and analysis of MEMS sensor based on piezoresistive effects. *Materials Science and Engineering: C*, vol. 27, pp. 691–694.

Kobayashi, R.; Nakamura, T.; Ogata, S. (2008): Development and implementation of recursive coarse-grained particle method for meso-scale simulation. *Materials transactions*, vol. 49, no. 11, pp. 2541–2549.

Kobayashi, R.; Nakamura, T.; Ogata, S. (2008): Development of hybrid atomistic/coarse-grained dynamic simulation approach. *Journal of Computational and Theoretical Nanoscience*, vol. 5, pp. 1768–1771.

Kondo, D.; Sato, S.; Awano, Y. (2008): Self-organization of novel carbon composite structure: Graphene multi-layers combined perpendicularly with aligned carbon nanotubes. *Applied Physics Express*, vol. 1, pp. 074003–1–3.

Ladd, A. (1994): Numerical simulations of particulate suspensions via discretized boltzmann equation, part 1. theoretical foundation. *Journal of Fluid Mechanics*, vol. 271, pp. 285–309.

Miller, R.; Tadmor, E. (2002): The quasicontinuum method: Overview, applications and current directions. *Journal of Computer-Aided Materials Design*, vol. 9, pp. 203–239.

Niu, X.; Shu, C.; Chew, Y.; Peng, Y. (2006): A momentum exchange-based immersed boundary-lattice Boltzmann method for simulating incompressible viscous flows. *Physics Letters A*, vol. 354, no. 3, pp. 173–182.

Novoselov, K.; Geim, A.; Morozov, S.; Jiang, D.; Zhang, Y.; Dubonos, S.; Grigorieva, I.; Firsov, A. (2004): Electric field effect in atomically thin carbon films. *Science*, vol. 306, pp. 666–669.

Ogata, S.; R. Kobayashi, R.; Gotoh, T. (2009): A suite of hybrid simulation schemes for nano-to-micrometer scale processes at solid-fluid interfaces. *Progress of Theoretical Physics Supplement*, vol. 178, pp. 149–156.

Peskin, C. (1977): Numerical analysis of blood flow in the heart. *Journal of Computational Physics*, vol. 25, no. 3, pp. 220–252.

Peskin, C. (2003): The immersed boundary method. *Acta Numerica*, vol. 11, pp. 479–517.

Rudd, R.; Broughton, J. (1998): Coarse-grained molecular dynamics and the atomic limit of finite elements. *Physical Review B*, vol. 58, no. 10, pp. 5893–5896.

Rudd, R.; Broughton, J. (2005): Coarse-grained molecular dynamics: Nonlinear finite elements and finite temperature. *Physical Review B*, vol. 72, no. 14, pp. 144104.

Succi, S. (2001): *The lattice Boltzmann equation for fluid dynamics and beyond*. Oxford University Press, USA.

Sukop, M.; Thorne Jr., J. (2006): *Lattice Boltzmann Modeling: Introduction for Geoscientists and Engineers*. Springer.

Tang, D.; Dowell, E. (2001): Effects of angle of attack on nonlinear flutter of a delta wing. *AIAA Journal*, vol. 39, pp. 15–21.

Yan, Y.; He, X.; Zhang, L.; Wang, Q. (2007): Flow-induced instability of double-walled carbon nanotubes based. *Journal of Applied Physics*, vol. 102, pp. 044307–1–8.

Zhang, J.; Childress, S.; Libchaber, A.; Shelley, M. (2000): Flexible filaments in a flowing soap film as a model for one-dimensional flags in a two-dimensional wind. *Nature*, vol. 408, pp. 835–839.

Zhang, Q.; Ruan, W.; Wang, H.; Zhou, Y.; Wang, Z.; Liu, L. (2010): A self-bended piezoresistive microcantilever flow sensor for low flow rate measurement. *Sensors and Actuators A: Physical*, vol. 158, pp. 273–279.

Zhu, L.; Peskin, C. (2003): Interaction of two flapping filaments in a flowing soap film. *Physics of Fluids*, vol. 15, pp. 128–136.